



Digitizing translucent object appearance by validating computed optical properties

DUC MINH TRAN,¹  MARK BO JENSEN,¹ PABLO SANTAFÉ-GABARDA,²  STEFAN KÄLLBERG,³ ALEJANDRO FERRERO,²  MORTEN RIEGER HANNEMOSE,¹  AND JEPPE REVALL FRISVAD^{1,*} 

¹Technical University of Denmark (DTU), 2800 Kongens Lyngby, Denmark

²Institute of Optics “Daza de Valdés”, Spanish National Research Council (IO-CSIC), 28006 Madrid, Spain

³Research Institutes of Sweden (RISE), 504 62 Borås, Sweden

*jerf@dtu.dk

Received 21 February 2024; revised 30 April 2024; accepted 30 April 2024; posted 30 April 2024; published 22 May 2024

The optical properties available for an object are most often fragmented and insufficient for photorealistic rendering of the object. We propose a procedure for digitizing a translucent object with sufficient information for predictive rendering of its appearance. Based on object material descriptions, we compute optical properties and validate or adjust this object appearance model based on comparison of simulation with spectrophotometric measurements of the bidirectional scattering-surface reflectance distribution function (BSSRDF). To ease this type of comparison, we provide an efficient simulation tool that computes the BSSRDF for a particular light-view configuration. Even with just a few configurations, the localized lighting in BSSRDF measurements is useful for assessing the appropriateness of computed or otherwise acquired optical properties. To validate an object appearance model in a more common lighting environment, we render the appearance of the obtained digital twin and assess the photorealism of our renderings through pixel-by-pixel comparison with photographs of the physical object. © 2024 Optica Publishing Group under the terms of the [Optica Open Access Publishing Agreement](#)

<https://doi.org/10.1364/AO.521974>

1. INTRODUCTION

In a broad range of manufacturing disciplines, each product has a digital twin useful for product design and quality assurance. The digital twin facilitates digital prototyping, a process that enables the designer to virtually explore use of materials before manufacturing starts. This saves time and reduces waste. However, if we are to trust and make decisions based on a digital twin, we need an ability to predictively render the appearance of the object it represents. We present a pipeline for creating digital twins from material characterization, appearance modeling of translucent materials, and validation from measurements.

The photorealism of a rendered image is often assessed implicitly by juxtaposition of a rendered image and a similar photograph, side-by-side, resulting in a visual search task of spotting the differences. A difficult task when comparing images with dense high-frequency details [1] as the visual working memory is limited to a few features at the time [2,3]. This means that when comparing two images the user needs to study each image and learn all the details that could potentially vary. It is not possible to know which details might vary *a priori* and details outside the locus of visual attention are not learned. Because of this, the viewer is forced to shift attention back and forth repeatedly looking for details to compare without knowing which details to focus on. In our validation, we align camera-based measurements with simulations to enable direct computation of

error metrics and difference images. We thus provide a method for quantitative assessment of the accuracy of an object appearance model on top of the commonly used qualitative assessment available through photo-render juxtaposition.

The bidirectional scattering-surface reflectance distribution function (BSSRDF) is a function for representing the appearance of a translucent object. The first primary facility for traceable measurements of the BSSRDF recently became available [4,5]. This enables us to validate the optical properties acquired for a translucent object by comparing simulation with measurements. While techniques for estimating optical properties often have a focus on a particular feature of light-matter interaction, such as the absorption and scattering coefficients [6–9], some methods strive for a more complete object digitization that enables photorealistic rendering [10,11]. Due to the lack of BSSRDF measurements, estimated optical properties of a translucent material are rarely validated. We describe the data needed to perform predictive rendering of a digital twin with an emphasis on procedures needed for validating the optical properties in these data and for assessing the photorealism of the predictively rendered images.

The BSSRDF encompasses both insurface and subsurface scattering [12]. The macroscopic shape together with the scattering and absorption properties of the interior of an object thus do not suffice for completely digitizing object appearance.

We demonstrate the use of acquired surface topography data for approximating the insurface scattering by estimating the microfacet normal distribution, which we insert in a bidirectional scattering distribution function (BSDF). We also test different choices of the directional distribution (phase function) used for the subsurface scattering and their influence on accurately capturing of the BSSRDF function. When our model better fits the BSSRDF measurements, we also obtain more photorealistic renderings.

2. RELATED WORK

A large body of literature is concerned with acquisition of the optical properties of materials. It is common to estimate optical properties based on spatially varying diffuse reflectance [8,9,13–15] or integrating sphere measurements [6,7,16]. An alternative approach is to compute optical properties based on a more microscopic description of the material [17,18]. This is the approach we take in this work. Regardless of how we obtain optical properties, we need a fairly complete coverage of the visible part of the spectrum to fully digitize the appearance of an object. We also need information about both insurface and subsurface scattering [12], and since the full object surface serves as the boundary of the subsurface scattering, we also need the full object shape [19,20]. We 3D scan the object surface and use surface topography measurements to estimate the insurface scattering.

In computer graphics, optical properties are acquired with the purpose of rendering realistic images [21]. The photorealism of an image rendered using acquired optical properties is however often left for the reader to judge from looking at the rendered image [22,23]. In some cases, the rendered image and a similar photograph are juxtaposed to assist the intuition of the reader [24–26]. Methods are available in optics that enable pixel-by-pixel comparison of photographed and rendered images [10,11]. With differentiable rendering [27,28], another option is to let an optimizer home in on the shape and the optical properties of the object observed in a photo [29]. This approach is however limited by the approximate material appearance models used for the differentiable forward simulation. In this work, we suggest use of sparse BSSRDF measurements for validating computed optical properties followed by use of a photo-render comparison for assessing the photorealism of the digitized object.

If we do not care about the optical properties of the material but simply want to capture the appearance of a specific produced item, the manufacturer's reference specimen, for example, we can use image-based techniques [30–33]. These approaches take advantage of neural networks to learn the appearance of an object from a set of input images. The light-view configurations these models can accurately predict the recorded object appearance for however depend on the captured data. Our use of computed optical properties makes our method useful for arbitrary light-view configurations. In addition, with optical properties computed from a microscopic description of the material, the digital twin retains a direct link to the material microstructure, such as size and type of surface microfacets and subsurface particles. This enables us to estimate the product

appearance consequence of changes in the microstructure due to changes in production.

3. MATERIALS AND METHOD

Figure 1 provides an overview of the different steps in our approach to digital twinning. Initially, we characterize the object of interest by collecting information on its micro and macro geometry as well as refractive indices of its different material constituents. The collected data serve as input for computing optical properties that describe scattering of light by surface microfacets and subsurface particles. These in turn serve as boundary conditions and input parameters for the radiative transfer equation, which we solve in simulation by Monte Carlo ray tracing. To acquire data for validation, we perform BSSRDF measurements and capture photographs of the object and the surrounding lighting environment. An object appearance model is validated by comparing simulations with BSSRDF measurements and rendered images with captured photographs. In the following sections, we describe the steps in more detail.

A. Object Characterization

The first step of the digitization pipeline is a characterization of the object of interest. We work with translucent objects manufactured by Covestro Deutschland AG. Using a caliper, we measured the outer dimension of the samples to be 149.1 mm × 104.5 mm × 6.35 mm.

1. Surface 3D Scan and Topography

In the development of digital twins, computer-aided design (CAD) models play a pivotal role, serving as a digital foundation for manufacturing processes before a physical prototype is created. However, there are instances where the digital representation of an object needs to be obtained from a physical copy. Various methods are available for scanning the surface of 3D objects, each with its own strengths and weaknesses. We use a structured light 3D scanner, ATOS III Triple Scan (GOM Metrology, Germany), with a stereo camera setup and a narrow-band blue light projector. The scanner projects a structured light pattern onto the object and uses triangulation to obtain surface points [34]. A high-resolution triangle mesh is then reconstructed from the surface points (possibly using screened Poisson reconstruction [35]). This triangle mesh is the output from the 3D scanner. The scanner boasts a maximum resolution of 0.01 mm, making it well suited for capturing detailed geometry of samples that are several centimeters in size.

An issue when 3D scanning the geometry of a translucent object is that the scanner can have difficulties detecting the actual surface and might instead detect subsurface scattering events [36]. One option to counteract this effect is to use a deep-learning-based diffusion model to estimate the signal from the true surface [37]. In our case, since we have samples exhibiting different levels of translucency, we worked around the problem by using the highly scattering sample IOL1068-07 for our scan of the object surface.

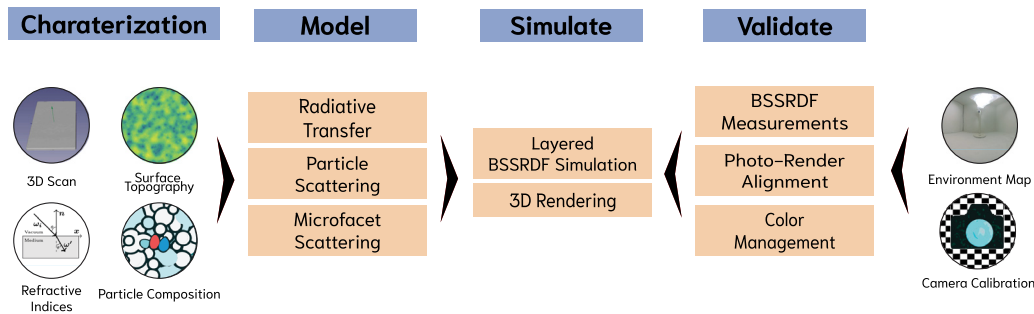


Fig. 1. Digitization and validation pipelines for generating digital twins of translucent objects.

Based on the bounding box of the mesh reconstructed from the 3D scan, the outer dimensions are $149.4 \text{ mm} \times 104.92 \text{ mm} \times 7.0 \text{ mm}$. The difference from the measured 6.35 mm is larger than expected. We found that this inaccuracy is due to outliers along the bottom edges (likely caused by a slight misalignment of subscans), which increased the outer dimension. To quantify the average error, we fitted planes to the top and bottom surfaces of the sample and computed the distance between them. The average thickness of the mesh computed in this way was 6.37 mm with a standard deviation of 0.046 mm , which is a reasonable deviation from the measured thickness.

Surface topography measurements were done with a coherent scanning interferometric (CSI) profilometer, Nexview NX2 (Zygo, CT, USA), which has six different objectives giving $1.4 \times$ to $100 \times$ magnifications. We used $20 \times$ magnification in our measurements, corresponding to $\Delta x / \Delta y$ pixel width/height of $0.871 \mu\text{m}$ and a Δz resolution of less than 1 nm . The spatial resolution was 1000×1000 pixels.

2. Refractive Indices and Particle Composition

The host medium of the Covestro objects is polycarbonate (PC) for which we assume a density of 1.2 g/mL . We use the complex refractive index of PC measured by Zhang *et al.* [38]. The real part of the refractive index was confirmed by the manufacturer. We have different versions of the object of interest with different particle inclusions. The manufacturer provided information on the particle weight percentages, mean diameter, and refractive

index at 550 nm . However, we need more information to compute the spectral optical properties of an object. We thus selected plausible spectral complex indices of refraction from the literature for the different particle inclusions. Table 1 lists the data we use for computing the optical properties of our samples.

B. Modeling Translucent Objects

Macroscopic models describing the appearance of a translucent object can be local or global [19,21]. The radiative transfer formulation where we describe the changes in radiance along a specific light path is the local formulation. The BSSRDF is the global formulation where we describe the observed radiance in some direction at some surface position due to an element of radiant flux incident in some surface position and from some direction. In this work, we use the local formulation to simulate expected observations in the global formulation. In the following, we describe the local radiative transfer formulation and how we, based on our object characterization, compute optical properties that serve as input parameters for this local path tracing model.

1. Radiative Transfer

For a ray of light $\mathbf{r}(s) = \mathbf{o} + s\vec{\omega}$ at the position \mathbf{o} in the direction $\vec{\omega}$ in a non-emitting turbid medium, we use the integral form of the radiative transfer equation to describe the radiance $L(s, \vec{\omega})$ at the distance s along the ray [41]:

Table 1. Different Samples of Our Object of Interest and Their Assumed Particle Inclusions Leading to Different Levels of Translucency^a

Sample	wt-% w_{particle}	Scattering Particle	Particle Density ρ_{particle}	Mean Diameter $[2r_{\text{min}}, 2r_{\text{max}}]$	Refractive Index n_{particle}
IOL1068-05	0.70	Titanium dioxide (TiO ₂)	4.23 g/mL	300 nm	[39]
IOL1068-06	3.00				
IOL1068-07	5.00				
IOL1068-08	0.30	Polydimethylsiloxane (PDMS)	0.965 g/mL	2.2 μm	[38]
IOL1068-09	0.65				
IOL1068-10	1.00				
IOL1068-11	1.50	Polyvinylpyrrolidone (PVP)	1.2 g/mL	[8 μm , 10 μm]	[40]
IOL1068-12	3.50				
IOL1068-13	5.00				
IOL1068-14	0.50	Polymethyl methacrylate (PMMA)	1.18 g/mL	[0.8 μm , 1 μm]	[38]
IOL1068-15	1.25				
IOL1068-16	2.00				

^aThe host medium is polycarbonate (PC) with refractive index n_{host} available from Zhang *et al.* [38].

$$L(s, \vec{\omega}) = L(0, \vec{\omega})e^{-\tau(0,s)} + \int_0^s e^{-\tau(s',s)} \int_{4\pi} \mu_s p(\vec{\omega}', \vec{\omega}) L(s', \vec{\omega}') d\omega' ds', \quad (1)$$

where μ_s is the scattering coefficient denoting the amount of scattering per distance unit as we move along the ray, while p is the phase function describing the distribution of the scattered light. We use boldface to denote positional vectors and arrow overline for unit length direction vectors. The optical depth from one point to another along the ray is defined by

$$\tau(s', s) = \int_{s'}^s \mu_t dt, \quad (2)$$

where $\mu_t = \mu_s + \mu_a$ is the extinction coefficient denoting the amount of scattering and absorption per distance unit (and μ_a is the absorption coefficient). These optical properties are independent of position in the medium for a homogeneous medium; then $\tau(s', s) = \mu_t(s - s')$, and the scattering coefficient is independent of the orientation of the object for an isotropic medium. The medium may still exhibit scattering anisotropy, which means that the phase function is not isotropic (and thus not constant).

In a medium with randomly oriented or spherical or very small particles, the phase function exhibits rotational symmetry around the forward direction, which means that $p(\vec{\omega}', \vec{\omega}) = p(\vec{\omega}' \cdot \vec{\omega})$. The Henyey–Greenstein phase function is commonly used [42]:

$$p_{\text{HG}}(\vec{\omega}' \cdot \vec{\omega}) = p_{\text{HG}}(\cos \theta) = \frac{1}{4\pi} \frac{1 - g^2}{(1 + g^2 - 2g \cos \theta)^{\frac{3}{2}}}, \quad (3)$$

where g is the asymmetry parameter (the mean cosine of the scattering angle) defined by

$$g = \int_{4\pi} (\vec{\omega} \cdot \vec{\omega}') p(\vec{\omega} \cdot \vec{\omega}') d\omega', \quad (4)$$

and the integration is over the full 4π solid angle of the unit sphere [as in Eq. (1)].

To compute input parameters (μ_s , μ_t , and p or g) for this radiative transfer model of light transport, we assume spherical light scattering particles and use the information available in Section 3.A.2 as input for the Lorenz–Mie theory [17,18]. This approach is covered next.

2. Particle Scattering

Lorenz [43] described the scattering of a plane wave of light by a transparent spherical particle in a transparent medium. Mie [44] formulated the theory for an electromagnetic plane wave scattered by an absorbing spherical particle in a transparent medium. This Lorenz–Mie theory is useful for computing the phase function p and the scattering and extinction cross sections C_s and C_t of a spherical particle of arbitrary size. For a known number density distribution N of particles in a medium, we can compute the scattering and extinction coefficients μ_s and μ_t using the corresponding cross sections [17].

Assuming independent scattering by the particles in the medium (decoupling approximation), we have for an interval of particle radii $r \in [r_{\min}, r_{\max}]$

$$\mu_{s|t} = \int_{r_{\min}}^{r_{\max}} C_{s|t}(r) N(r) dr, \quad (5)$$

where $s|t$ denotes that the equation is valid for either of the subscripts s or t , and we can find N using the following relation between weight percentage (wt-%) of the particle inclusion w_{particle} , particle and host densities ρ_{particle} and ρ_{host} , and the interval of particle radii:

$$\frac{4\pi}{3} \int_{r_{\min}}^{r_{\max}} r^3 N(r) dr = \frac{w_{\text{particle}}/\rho_{\text{particle}}}{100/\rho_{\text{host}}}. \quad (6)$$

The data needed to compute N for our samples using this relation are in Table 1.

The Lorenz–Mie theory is parameterized by the size parameters

$$x = \frac{2\pi r n_{\text{host}}}{\lambda}, \quad y = \frac{2\pi r n_{\text{particle}}}{\lambda}, \quad (7)$$

where n_{host} and n_{particle} are the refractive indices of the host medium and the particle, and λ is the wavelength of the light *in vacuo*. With these size parameters, we can compute the Lorenz–Mie coefficients a_n and b_n , and these are the key to computing the optical properties using truncated series expansions. Specifically, we have [17,18,45]

$$C_s = \frac{\lambda^2}{2\pi |n_{\text{host}}|^2} \sum_{n=1}^{\infty} (2n+1) (|a_n|^2 + |b_n|^2), \quad (8)$$

$$C_t = \frac{\lambda^2}{2\pi} \sum_{n=1}^{\infty} (2n+1) \text{Re} \left(\frac{a_n + b_n}{n_{\text{host}}^2} \right), \quad (9)$$

$$S_1(\cos \theta) = \sum_{n=1}^{\infty} \frac{2n+1}{n(n+1)} (a_n \pi_n(\cos \theta) + b_n \tau_n(\cos \theta)), \quad (10)$$

$$S_2(\cos \theta) = \sum_{n=1}^{\infty} \frac{2n+1}{n(n+1)} (a_n \tau_n(\cos \theta) + b_n \pi_n(\cos \theta)), \quad (11)$$

where Re takes the real part of a complex number while $\pi_n(\cos \theta) = P_n^1(\cos \theta)/\sin \theta$ and $\tau_n(\cos \theta) = dP_n^1/d\theta$, with P_n^1 the first order associated Legendre polynomial. For unpolarized light, the phase function is

$$p_{\text{LM}}(\cos \theta) = \frac{|S_1(\cos \theta)|^2 + |S_2(\cos \theta)|^2}{4\pi \sum_{n=1}^{\infty} (2n+1) (|a_n|^2 + |b_n|^2)}. \quad (12)$$

For an absorbing particle, y becomes a complex number. For an absorbing host, x becomes a complex number and the host absorption needs to be added to the extinction coefficient computed using Eqs. (5) and (9). The Lorenz–Mie coefficients a_n and b_n become numerically more difficult to compute for complex size parameters. To have a robust numerical computation for complex x and y , we use the method by Frisvad *et al.* [45].

Since the Lorenz–Mie phase function is a truncated series expansion, it easily becomes computationally demanding to evaluate the function for every scattering event in a turbid medium. A commonly used option is then to compute the asymmetry parameter g directly from the Lorenz–Mie coefficients [17,45]:

$$g = \frac{\sum_{n=1}^{\infty} \left[\frac{n(n+2)}{n+1} \operatorname{Re}(a_n a_{n+1}^* + b_n b_{n+1}^*) + \frac{2n+1}{n(n+1)} \operatorname{Re}(a_n b_n^*) \right]}{\frac{1}{2} \sum_{n=1}^{\infty} (2n+1)(|a_n|^2 + |b_n|^2)}, \tag{13}$$

where the asterisk $*$ denotes the complex conjugate. This g is then used in the Henyey–Greenstein phase function p_{HG} as an inexpensive approximation. To enable use of the actual Lorenz–Mie phase function in simulation, we tabulate the function for a given particle type.

From the information in Table 1, we computed the bulk optical properties of our samples for wavelengths from 380 nm to 780 nm in steps of 10 nm. Table 2 lists the computed optical properties at $\lambda = 550$ nm (the full spectral optical properties are available at [46]). With these optical properties, we can simulate subsurface scattering, but we also need to model how light enters and exits the medium. The insurface scattering described in the following section models these boundary conditions.

3. Microfacet Scattering

The range of available surface BSDFs is diverse. We use the Torrance–Sparrow model [47] extended to include refraction [48,49] to model a single insurface scattering event. The model fits well to measured data for relatively smooth surfaces [49] but suffers from energy loss as the roughness increases (due to the single-scattering assumption). To deal with this problem, an extension has been developed to let the model include multiple insurface scattering events [50]. In the supplemental material for their work, Heitz *et al.* [50] provide an extensive analysis of the model’s correctness in the case of dielectrics for various relative refractive indices and various angles of incidence. They present full distributions over observation angles compared with Monte Carlo simulations and provide results for one, two, and three scattering events (bounces). The version of the model we use corresponds to their one bounce results. For a surface with a Beckmann microfacet normal distribution and a roughness of 0.2, the error of the model we use is vanishing for angles of

Table 3. Percentage of the BSDF Explained by the Single-Scattering Microfacet Model for Different Roughness Values α and Angles of Incidence When Using a Relative Refractive Index of 1.4 and a Beckmann Distribution of Surface Normals^a

θ_i	α			
	0.2	0.4	0.6	0.8
0.0°	1.000	1.000	0.995	0.985
11.5°	1.000	0.999	0.994	0.984
22.9°	1.000	0.998	0.991	0.979
34.4°	1.000	0.995	0.984	0.972
45.8°	1.000	0.988	0.975	0.963
57.3°	0.996	0.975	0.964	0.947
68.8°	0.977	0.959	0.950	0.911
80.2°	0.946	0.958	0.922	0.815
85.9°	0.958	0.967	0.875	0.686

^aThe numbers are based on data from Heitz *et al.* [50].

incidence of less than 45° and a relative refractive index in [0.9, 1.8]. Their investigation is summarized for a relative refractive index of 1.4 in Table 3.

Low roughnesses are unfortunately not included in the analysis by Heitz *et al.*, but other work [51] based on the GGX normal distribution (see below) found a vanishing loss of energy in the model for roughnesses of 0.035 and 0.125. When using this type of geometric optics model with measured surface topography, Wittmann *et al.* [52] found that the model can fit measured gloss well for low roughness even at very grazing angles as long as the spatial period of the roughness is larger than the wavelength of the light (800 nm). Our samples have rather smooth surfaces, and we measure the surface topography with a pixel size larger than the wavelength (871 nm). The single-scattering microfacet BSDF model thus seems sufficient for our purposes.

The Torrance–Sparrow model considers the microfacets of the surface perfectly smooth and describes them by a distribution D of microfacet surface normals \vec{m} around the macroscopic surface normal \vec{n} in the surface position of interest. The BSDF $f_s = f_r + f_t$ with f_r describing reflection mode and f_t transmission mode is then [49]

$$f_r(\vec{\omega}_i, \vec{\omega}_o) = \frac{F(\vec{\omega}_i \cdot \vec{m}_r) G(\vec{\omega}_i, \vec{\omega}_o) D(\vec{m}_r \cdot \vec{n})}{4|\vec{\omega}_i \cdot \vec{n}| |\vec{\omega}_o \cdot \vec{n}|}, \tag{14}$$

Table 2. Computed Bulk Optical Properties at $\lambda = 550$ nm Using Lorenz–Mie Theory with Information from Table 1

Sample	Scattering μ_s (m ⁻¹)	Absorption μ_a (m ⁻¹)	Asymmetry g	Refractive Index n_{bulk}
IOL1068-05	29313.0	11.720	0.68389	1.5898
IOL1068-06	125630.0	19.598	0.68389	
IOL1068-07	209380.0	26.448	0.68389	
IOL1068-08	6781.1	9.4557	0.97358	1.5889
IOL1068-09	14692.0	9.6116	0.97358	
IOL1068-10	22604.0	9.7676	0.97358	
IOL1068-11	5064.4	10.260	0.99426	1.5889
IOL1068-12	10129.0	11.197	0.99426	
IOL1068-13	16881.0	12.448	0.99426	
IOL1068-14	3379.7	9.3422	0.95883	1.5885
IOL1068-15	8449.3	9.3725	0.95883	
IOL1068-16	13519.0	9.4028	0.95883	

$$f_i(\vec{\omega}_i, \vec{\omega}_o) = \frac{|\vec{\omega}_i \cdot \vec{m}_t| |\vec{\omega}_o \cdot \vec{m}_t| n_o^2 (1 - F(\vec{\omega}_i \cdot \vec{m}_t)) G(\vec{\omega}_i, \vec{\omega}_o) D(\vec{m}_t \cdot \vec{n})}{|\vec{\omega}_i \cdot \vec{n}| |\vec{\omega}_o \cdot \vec{n}| (n_i(\vec{\omega}_i \cdot \vec{m}_t) + n_o(\vec{\omega}_o \cdot \vec{m}_t))^2}, \quad (15)$$

where light is incident from a medium of refractive index n_i and scatters into a medium of refractive index n_o . The term F denotes Fresnel reflectance for unpolarized light and G is a geometric attenuation term representing how microfacets shadow and mask each other. The microfacet normals in these equations are the ones leading to the direction of perfect reflection or transmission:

$$\vec{m}_r = \frac{\vec{\omega}_i + \vec{\omega}_o}{\|\vec{\omega}_i + \vec{\omega}_o\|}, \quad \vec{m}_t = -\frac{n_i \vec{\omega}_i + n_o \vec{\omega}_o}{\|n_i \vec{\omega}_i + n_o \vec{\omega}_o\|}. \quad (16)$$

The most common choice for G is the Smith model [49,53]. For D , common choices are the Beckmann distribution [47,54], which is based on a normal distribution, and the Trowbridge–Reitz (TR) distribution [55] (sometimes called GGX [49]).

The main difference between the Beckmann and the TR distributions is that TR has slightly heavier tails, which often fits empirical data better [49,55,56]. Both are parameterized by a roughness parameter α that describes the standard deviation of the distribution. The TR distribution is given by

$$D_{\text{TR}}(\cos \theta_m) = \frac{\alpha^2 H(\cos \theta_m)}{\pi (\alpha^2 - 1 \cos^2(\theta_m) + 1)^2}, \quad (17)$$

where $\cos \theta_m = \vec{m} \cdot \vec{n}$ and $H(\cdot)$ is the Heaviside step function (one for positive argument and zero otherwise).

To acquire a microfacet normal distribution for our object of interest, we measure surface height maps for samples IOL1068-07 and IOL1068-08 (see Fig. 2). The spatial resolution is 1000×1000 pixels, with each pixel representing an area of $0.871 \mu\text{m} \times 0.871 \mu\text{m}$. From the measurements, the surface of IOL1068-07 is smoother with a root mean square height of $S_q = 41.741 \text{ nm}$, while IOL1068-08 has $S_q = 127.89 \text{ nm}$. This correlates well with the particle sizes of the two sample types: IOL1068-07 with the smaller particle size has a smoother surface.

To compute a normal distribution from the measurements, we follow the plane fitting approach of Dong *et al.* [57] and apply a Gaussian kernel with standard deviation $\sigma = 0.871^{-1} \mu\text{m}$ and a kernel size of 15×15 pixels. Like Dong *et al.* [57], we find that variation in these parameters does not significantly affect the resulting normal distribution. We fitted the TR and Beckmann distributions to the measured normalized distribution of normals. Table 4 lists the fitted parameters, while Figs. 2(c) and 2(d) show the fitted distributions. Note that similar to Walter *et al.* [49] we also include a scale parameter in our fit. For the smoother sample we found that Beckmann provides a lower mean-squared error (MSE), while TR has a lower MSE for the rougher sample.

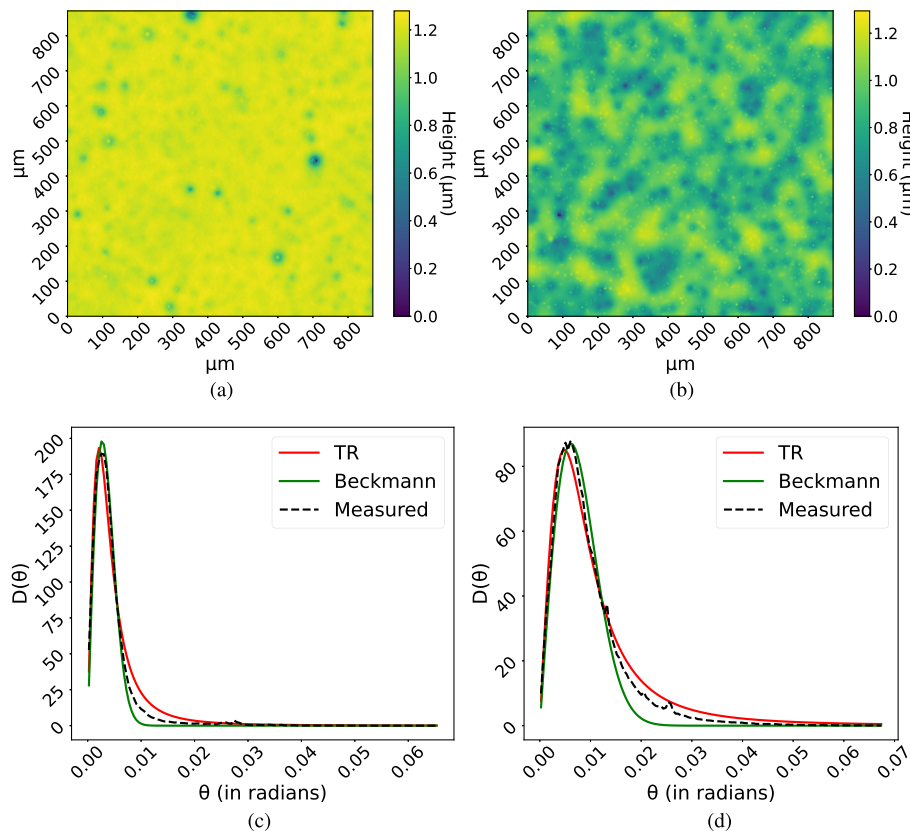


Fig. 2. Measured heightmap and fitted to microfacet model for samples IOL1068-07 and IOL1068-08. Beckmann fits better around the peak for IOL1068-07 while TR captures the heavier tails for IOL1068-08 better. The fitted parameters are shown in Table 4.

Table 4. Fitted Parameters to Measured Surface Normal Distribution for IOL1068-07 and IOL1068-08

Sample	Model	α	Scale	MSE
IOL1068-07	TR	0.0037	1.0948	10.609
	Beckmann	0.0038	0.8883	6.9014
IOL1068-08	TR	0.00836	1.095	2.3895
	Beckmann	0.00866	0.8790	4.853

C. Light Transport Simulation

To simulate the appearance of a translucent object, we need to evaluate the radiant flux Φ_p received in the pixel of a camera. The camera measures received radiant energy. Dividing by the exposure time, we obtain the received radiant flux. The measurement equation for what the camera sees in a pixel of area A_p and solid angle ω_p is then

$$\Phi_p = \int_{A_p} \int_{\omega_p} L_p(\mathbf{x}_p, \vec{\omega}_p) \cos \theta_p d\omega_p dA_p, \quad (18)$$

where $\mathbf{x}_p \in A_p$ is a position in the light sensitive cavity of the pixel and $\cos \theta_p \approx 1$ is the cosine of the angle between the direction where the radiance came from $\vec{\omega}_p$ and the center direction of the pixel solid angle. We collect the incident radiance L_p as outgoing radiance L_o from a position \mathbf{x} in the direction $\vec{\omega}_o = -\vec{\omega}_p$ using

$$L_o(\mathbf{x}, \vec{\omega}_o) = L_e(\mathbf{x}, \vec{\omega}_o) + \int_{4\pi} f_i(\vec{\omega}_i, \vec{\omega}_o) L_i(\mathbf{x}, \vec{\omega}_i) |\vec{\omega}_i \cdot \vec{n}| d\omega_i, \quad (19)$$

where L_e is emitted radiance and L_i is incident radiance collected from elsewhere in the scene or from subsurface scattering. The incident radiance arriving at the surface of the translucent object from inside would be $L(s, -\vec{\omega}_i)$ in Eq. (1), whereas $L(0, \vec{\omega}_o)$ for some ray along the subsurface scattering path would be L_o from Eq. (19) evaluated at the point of entry. The integrals in Eqs. (18), (19), and (1) are evaluated by Monte Carlo integration. To simplify the integral in Eq. (18), we assume an orthographic or a pinhole camera model. These models have only one valid direction of observation for every \mathbf{x}_p . The camera then measures the intensity in a pixel I_p instead of radiant flux:

$$I_p = \int_{A_p} L_p(\mathbf{x}_p, \vec{\omega}_p) dA_p, \quad (20)$$

with $\vec{\omega}_p$ constant for an orthographic camera model and $\vec{\omega}_p = \frac{\mathbf{x}_p - \mathbf{x}_e}{\|\mathbf{x}_p - \mathbf{x}_e\|}$ for a pinhole camera model, as all observed light rays are expected to converge toward one eye point \mathbf{x}_e in this model.

For more efficient Monte Carlo integration of Eq. (1), importance sampling of the exponential attenuation and the Henyey–Greenstein phase function is available from Pharr *et al.* [58]. Similarly, Walter *et al.* [49] provide importance sampling for the surface BSDF. We tabulate the Lorenz–Mie phase function using a table of $2^{12} = 4096$ entries. Using the table for importance sampling is the same procedure as described for simpler phase functions [59].

1. Layered BSSRDF Simulation

To compare with BSSRDF measurements, we assume a plane-parallel medium with its outer surface in the xy -plane and

thickness along the z -axis. In this simulation, we have pre-selected the wavelength λ and the directions of incidence and observation, $\vec{\omega}_i$ and $\vec{\omega}_o$. We compute (for a perfectly smooth surface) or sample (for $\alpha > 0$) a direction of light $\vec{\omega}_{21}$ that will refract toward the direction of observation. We then start our Monte Carlo path tracing from the source by sampling L_i from a measured map of incident radiance. This is important to make our simulation comparable to BSSRDF measurements. Any subsurface scattering event along a path can in the direction $\vec{\omega}_{21}$ only contribute to one surface point \mathbf{x}_o . If the relevant surface point is seen in a pixel, we explicitly compute the contribution using

$$L_o(\mathbf{x}_o, \vec{\omega}_o) = f_s(-\vec{\omega}_{21}, \vec{\omega}_o) e^{-\mu_t \|\mathbf{x}_o - \mathbf{x}_s\|} \frac{e^{-\mu_s s} \mu_s}{\text{pdf}(s)} \times p(\vec{\omega}_s, \vec{\omega}_{21}) L(\mathbf{x}_s, \vec{\omega}_s), \quad (21)$$

where $\mathbf{x}_s = \mathbf{o} + s \vec{\omega}_s$ is the position of a scattering event along a ray in the turbid medium and s is the distance to this scattering event typically sampled using $\text{pdf}(s) = e^{-\mu_t s} \mu_t$. With this sampling, the fraction in Eq. (21) simplifies to the single scattering albedo μ_s / μ_t . This connection of a scattering event to an observed point corresponds to splitting the integral in Eq. (1) into a randomly sampled part and a directly evaluated part. Since we cannot sample the exact direction $\vec{\omega}_{21}$ by chance (the probability of sampling a specific direction is zero), this is a valid split of the linear integration operator.

Using progressive updates of the Monte Carlo estimated intensity received in each pixel of an orthographic camera observing the xy -plane, our simulator collects radiance from a specified direction $\vec{\omega}_o = -\vec{\omega}_p$. The BSSRDF values resulting from our simulation are then

$$f_{\text{ssr}}(\mathbf{x}_i, \vec{\omega}_i; \mathbf{x}_o, \vec{\omega}_o) = \frac{dL_{\text{ssr}}(\mathbf{x}_i, \vec{\omega}_i; \mathbf{x}_o, \vec{\omega}_o)}{d\Phi_i(\mathbf{x}_i, \vec{\omega}_i)} \approx \frac{I_p}{A_{\perp} \Phi_i}, \quad (22)$$

where $A_{\perp} = A_o \cos \theta_o$ is a constant projected area with A_o the surface area observed in a pixel and θ_o the angle of observation ($\cos \theta_o$ is the z -component of $\vec{\omega}_o$), and Φ_i is the incident flux from the selected direction $\vec{\omega}_i$, which we obtain by integrating our measured map of incident radiance L_i while letting the origin of the coordinate system represent \mathbf{x}_i . An online version of our simulator is available at [60].

2. Realistic Rendering in 3D

To render an image of a 3D object, we use the triangle mesh surface representation (Section 3.A.1) and solve the same set of Eqs. (1), (19), and (20) using Monte Carlo integration [58,61]. In this case, however, we do not explicitly connect to the surface, as it is not obvious what point and direction to connect with. Instead, we model the incident illumination using an environment map. This is an image representing incident light from all directions surrounding the scene. For each pixel, we trace a path starting from the camera. When a ray in this path is not inside the translucent object and does not hit an object in the scene, it receives radiance from the environment map. This type of rendering algorithm is referred to as unidirectional path tracing. To perform efficient ray-triangle intersections on the graphics

processing unit (GPU), we use OptiX [62] (NVIDIA, CA, USA). Since the environment map is captured using an RGB camera and because the images we capture with are captured using an RGB camera, we convert our spectral optical properties to representative RGB vectors [10,45] using weighted averages with weights from the RGB color matching functions listed by Stockman and Sharpe [63]. When a path enters a translucent object, we sample one color band (R, G, or B) with equal probability and consider only the optical properties of this color band for the rest of the path. The other color bands are zeroed out and the result for the sampled band is divided by the probability. This significantly simplifies the Monte Carlo integration of Eq. (1), as we can then do very good importance sampling.

D. Validation

Our validation is in two parts: a validation of our model's ability to predict reflectance for specific light-view configurations based on comparison to BSSRDF measurements and a photo-renderer comparison enabling us to assess how well our model captures the overall appearance of the translucent object. We first describe the acquisition of data for the comparisons and provide the results of the comparisons in Section 4.

1. BSSRDF Measurements

To measure the BSSRDF, we used the primary facility at the *Instituto de Óptica "Daza de Valdés"* (IO-CSIC, Spain). This is a camera-based goniospectrophotometer, allowing irradiance and collection directions to be realized with a six-axis robot arm to move the sample, and a rotatory stage to move the camera around it. An overview of the setup is in Fig. 3. The facility is described by Santafé-Gabarda *et al.* [4] and in this work we include the upgrades described in a comparison of the BSSRDF measurement scale of the setup with that of a setup developed at *Conservatoire National des Arts et Métiers* (CNAM, France) [5]. The source of our setup is a stable laser-driven light source (LDLS) with a small irradiated area on the sample surface. In our measurements, the irradiated area has a full width at half maximum (FWHM) of approximately 200 μm . The camera is

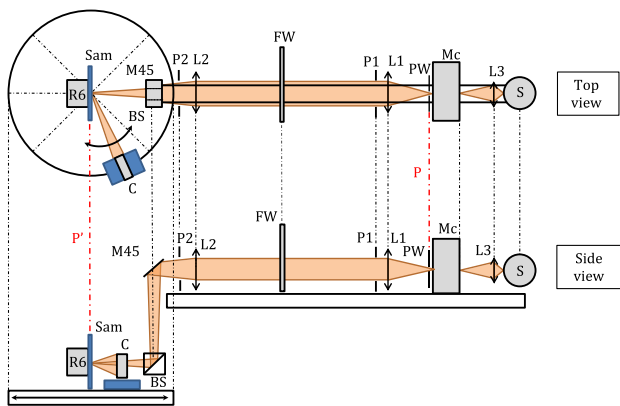


Fig. 3. Diagram of the BSSRDF measurement setup at IO-CSIC [4,5]. BS, beam splitter; C, camera; FW, filter wheel; L3, lens 3 (35 mm); L1, lens 1 (250 mm); L2, lens 2 (1 mm); M45, mirror at -45° ; Mc, monochromator; P, object principal plane; P', image principal plane; P1, diaphragm1; P2, diaphragm2; PW, pinhole wheel; R6, six-axis robot; Sam, sample; S, source.

a high-sensitivity complementary metal-oxide-semiconductor (CMOS) camera with a high spatial resolution and low readout noise. In our measurements, the sample surface area observed by the camera is approximately $100 \mu\text{m} \times 100 \mu\text{m}$. The system performs SI-traceable BSSRDF measurements with relative expanded uncertainties ($k = 2$) below 5%.

Together with this setup, we used the following measurement equation derived from the definition of the BSSRDF [the first equality in Eq. (22)]:

$$f_{\text{ssr}}^r(A_i, \vec{\omega}_i; \mathbf{x}_o, \vec{\omega}_o) = \frac{\Phi_o(\mathbf{x}_o, \vec{\omega}_o)}{A_{\perp} \omega_o \Phi_i(A_i, \vec{\omega}_i)}, \quad (23)$$

where ω_o is the collection solid angle and $A_{\perp} = A_o \cos \theta_o$ is the projected area observed by a camera pixel. These are constants while $\Phi_o(\mathbf{x}_o, \vec{\omega}_o)$ is the outgoing radiant flux at the location \mathbf{x}_o in the direction $\vec{\omega}_o$. We obtain $\Phi_i(A_i, \vec{\omega}_i)$, which represents flux incident at \mathbf{x}_i , by integrating a map of incident radiance L_i across the small area of incidence A_i surrounding \mathbf{x}_i . The map of L_i is acquired by rotating the camera to directly observe the source and performing a measurement μm without a sample.

2. Photo-Render Alignment and Color Management

To document the appearance of our samples, we capture photographs. Since our goal is to use these photographs as reference images for validation of our object appearance model, we perform camera calibration and capture the lighting environment as well.

We use the back camera of an iPhone 15 Pro (Apple, CA, USA) to capture reference images and use the calibration tool in MATLAB (MathWorks, MA, USA) to estimate camera matrix and lens distortion [64]. To capture the high-dynamic-range (HDR) lighting environment, we use an Insta360 Pro 2 camera (Insta360, CA, USA). Because we use two different cameras, we need to color calibrate both to ensure that they are in the same color space. To this end, we capture all images in RAW format and perform an initial step where we capture images of an X-Rite ColorChecker Passport Photo 2 (X-Rite, MI, USA) with both cameras. We use these photos with the ColorChecker Camera Calibration application to obtain a calibration matrix that maps from camera RGB to CIE XYZ values, assuming a D50 illuminant. Once CIE XYZ values are available, we can convert the image data to CIE RGB, which is the color space we use for rendering in 3D. In this way, we ensure a meaningful comparison of radiometric quantities as we then have both the optical properties of the samples (see Section 3.C.2) as well as the reference images and the captured HDR environment in the CIE RGB color space.

To show the translucency of the sample, we position the sample on a checkerboard and manually align the top left corner to the checkerboard grid. When capturing the images, we also capture a corresponding image of the checkerboard where the sample is not present. We include the image of the checkerboard without the sample in the camera calibration images. As the camera calibration process involves estimating the poses of all checkerboards relative to the camera, we also obtain the pose of the checkerboard on which the sample is positioned, which is needed for the subsequent rendering of the digital twins. The pose of the sample relative to the checkerboard is obtained by

assuming the top left corner of the sample is perfectly aligned with the rendered checkerboard.

The height and width of the checkerboard squares are 2 cm, and we assume a planar surface with diffuse reflection. We determined the reflectances of the checkerboard using a VideometerLab 4 (Videometer, Denmark), which is an integrating sphere equipped with a camera and internal sources at multiple spectral bands. This instrument is useful for capturing spectral bihemispherical diffuse reflectance. We converted the spectral data into a CIE RGB texture for rendering our checkerboard surface.

Scene illumination is achieved using the captured environment map (see Section 3.C.2). HDR environment maps usually represent a source of light assumed to be infinitely distant. However, to account for light distance fall-off in our capture setup, we project our HDR onto a sphere with a 60 cm radius, measured from the light source to the top of the sample. During rendering, we position the sample so that its top aligns with the center of the sphere. To ensure matching illumination, we scale the environment map's radiance, aligning the checkerboard's diffuse reflection with our reference photograph. Additionally, we undistort our reference images. Despite these measures, it is important to acknowledge that camera calibration inherently involves some re-projection error, and recreating a physical scene inevitably introduces a small degree of misalignment.

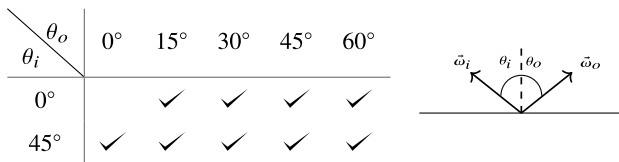


Fig. 4. Angular configurations of BSSRDF measurements. The azimuthal angles were $\phi_i = 0^\circ$ and $\phi_o = 180^\circ$.

4. RESULTS

In this section, we focus on validation results for two samples: IOL1068-08 and IOL1068-09. These two samples contain the same scattering particles and vary only in weight percentages.

A. BSSRDF Validation

To validate our model for specific light-view configurations, we measured the BSSRDF of our samples using the method described in Section 3.D.1. The spatial resolution of our measurements is 117×117 pixels with a pixel size of $0.1029 \text{ mm} \times 0.1029 \text{ mm}$. We measured each sample at the angular configurations listed in Fig. 4. All our measurements were performed for $\lambda = 550 \text{ nm}$ and in reflection mode, i.e., $\vec{\omega}_i \cdot \vec{\omega}_o > 0$.

We simulated BSSRDF slices with both tabulated Lorenz–Mie phase functions and analytic Henyey–Greenstein (HG) phase functions using the asymmetry parameter g specified in Table 2. The simulations were performed at a spatial resolution of 259×259 , and we subsequently cropped the central region to achieve a final resolution of 117×117 pixels, aligning with the resolution of the measurement for direct comparison.

Figure 5 shows the BSSRDF slices obtained from measurements and simulations. The result highlights the limitations of the HG phase function, particularly its restriction to fairly elliptical-shaped scattering distributions, which are not able to match the side-scattering shape of the Lorenz–Mie phase function. This difference is best seen for IOL1068-09, which has a higher scattering coefficient where the scattering shape is more noticeable. The difference in phase functions is shown in Fig. 6, where polar plots of the phase function reveal that Lorenz–Mie theory captures subtle side-scattering effects. However, the Lorenz–Mie phase function is not perfect; it has slightly too much side-scattering compared to the measurements, also most evident for sample IOL-1068-09. The slight mismatch is partly due to a lack of information about the particle size distribution.

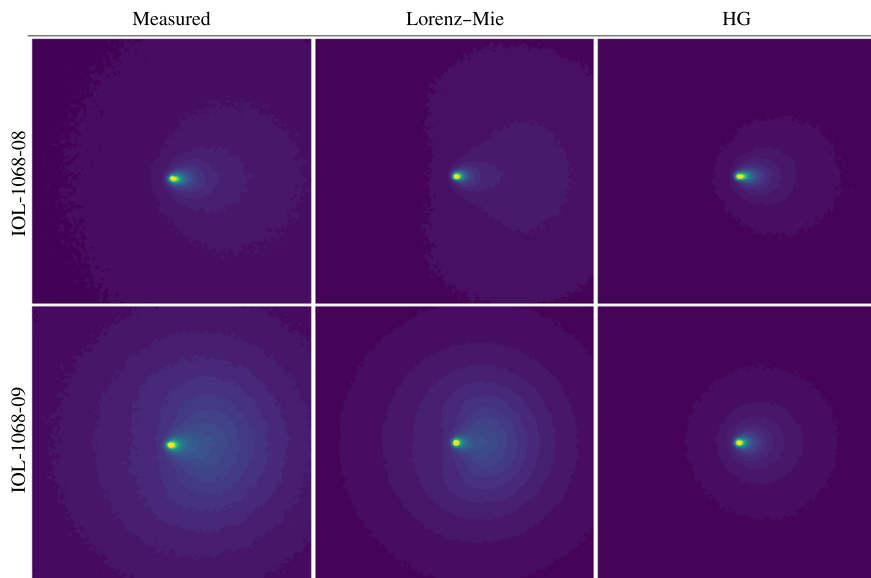


Fig. 5. Normalized false color plots of BSSRDFs with optical properties from Table 2. The shown area is $12.0 \text{ mm} \times 12.0 \text{ mm}$ and the angular configuration is $\theta_i = 45^\circ$ and $\theta_o = 0^\circ$.

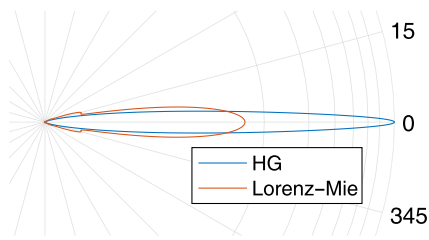


Fig. 6. Cross-section polar plots of Lorenz-Mie phase function and HG with $g = 0.9715$ from Table 2 for samples IOL1068-08 and IOL1068-9.

We computed the phase function based on the mean particle radius, while a distribution of particle radii is usually used for computing the phase function. With incomplete information about the material, a discrepancy between BSSRDF slices is expected.

The shape of the BSSRDF isocontours is an important aspect, but the overall quantity of reflected energy is equally important. Examining the profile along the plane of incidence (the line of pixels through the center of a BSSRDF slice) in Fig. 7, disparities emerge between the two samples. In the case of IOL1068-08, the simulated curves align well with the measurements. However, variations in the peak are observed due to the narrowness of the beam, leading to fluctuations depending on the targeted surface area. The application of a statistical microfacet model averages out the reflectance over a larger area. Since our beam has an FWHM of $200 \mu\text{m}$, it might hit a point on the surface that is near the specular lobe leading to fluctuations within the irradiated area. Therefore, precise comparisons within the irradiated area with such a narrow beam prove challenging. It is worth noticing that the two angular configurations, $\theta_i = 45^\circ, \theta_o = 0^\circ$ and $\theta_i = 0^\circ, \theta_o = 45^\circ$, exhibit symmetry, as predicted by light transport theory.

For IOL1068-09, we see a considerable over-prediction of reflected energy, despite the relatively matching BSSRDF shape. This discrepancy is attributed to the inherent challenges

in estimating optical properties accurately. In this complex estimation process, identifying the source of error is challenging due to missing information. One likely reason is that, while Lorenz-Mie theory is a physically correct model, our model still relies on assumptions. Due to our assumption of independent scattering by the particles, we effectively neglect particle-particle interference effects, which as the scattering increases become less viable. To quantitatively assess the disparities, we computed the mean squared relative error (MSRE) over the measured surface area, also detailed in Table 5. The table illustrates that the MSRE is notably higher for IOL1068-09. In Section 5.B we will try to correct this over-estimation such that it matches the measurements. This section showed how BSSRDF measurements can be used as a tool for validating optical properties and identifying discrepancies.

B. Appearance of the Digital Twin

In this section, we render the appearance of our digital twin. We use the optical properties as computed within $380\text{--}780 \text{ nm}$ converted to RGB vectors (see Section 3.C.2).

1. Rendering Scene Setup

Figure 8 shows the rendered image for the Lorenz-Mie phase function for the sample IOL1068-08 and compares the rendering to a photograph. The presence of misalignment of the checkboard pattern is evident in the error images due to the assumption of a perfectly planar surface. Neglecting these small misalignments we can focus on the sample instead. The results show a good correspondence with the photograph. There is a slight amount of over-scattering on the red channel, resulting in brighter black dice and a slight color shift. This error is most likely due to using the extinction coefficient from [38]. However, despite this color shift, the level of translucency matches the photograph well.

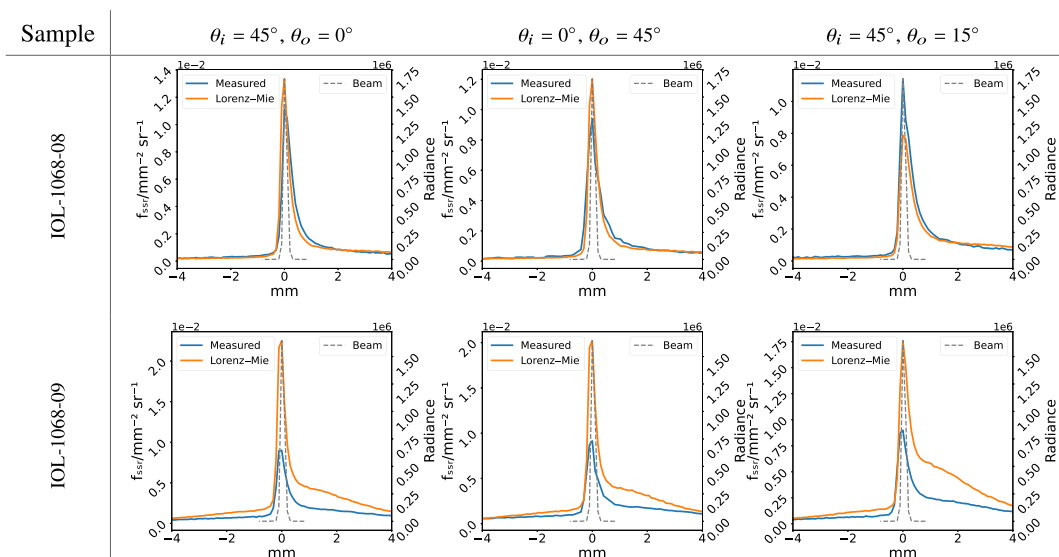


Fig. 7. Cross section along the plane of incidence from Fig. 5 with Lorenz-Mie phase function. The beam profile is shown with a dashed line and plots incident radiance using the axis on the right-hand side.

Table 5. Sum of Radiance from Simulations and Measurements^a

Sample		Angular Configuration		
		$\theta_i = 45^\circ, \theta_o = 0^\circ$	$\theta_i = 0^\circ, \theta_o = 45^\circ$	$\theta_i = 45^\circ, \theta_o = 15^\circ$
IOL1068-08	Measured	4.655	4.291	5.002
	Simulated	4.601 (0.162)	4.145 (0.162)	4.747 (0.240)
IOL1068-09	Measured	8.295	9.982	8.578
	Simulated	13.144 (0.545)	11.856 (0.346)	12.673 (0.661)

^aThe mean squared relative error (MSRE) for simulation against measured BSSRDF in Fig. 5 is denoted in parenthesis.

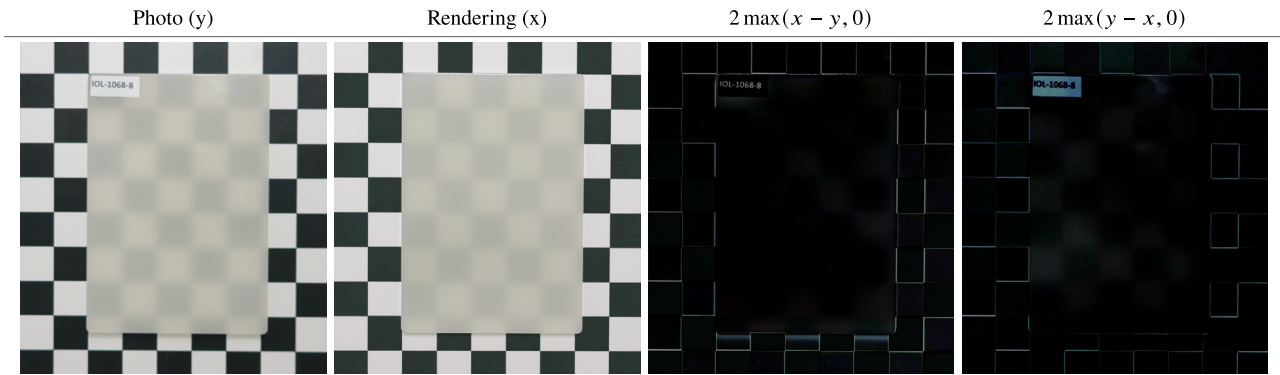


Fig. 8. Rendering of sample IOL1068-08 with the Lorenz–Mie phase function and a photograph of the sample. The RMSE is 0.05219 and the SSIM is 0.864.

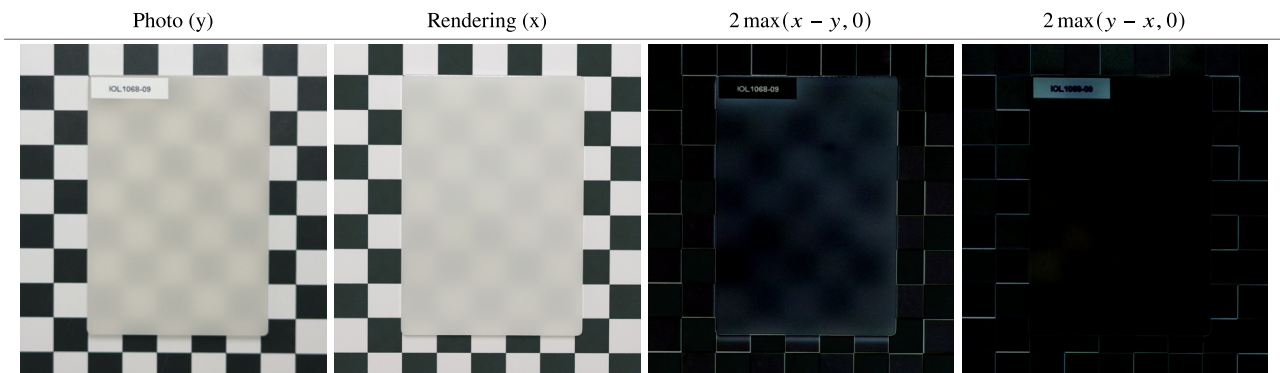


Fig. 9. Rendering of sample IOL1068-09 with the Lorenz–Mie phase function and a photograph of the sample. The RMSE is 0.0591 and the SSIM is 0.859. There is an overestimation of the scattered light in the rendered image in correspondence to BSSRDF simulations resulting in a rendering with too much reflectance.

On the other hand, Fig. 9 shows a clear overestimation, resulting in a too-bright rendering. This is in alignment with the BSSRDF measurements, which also showed an overestimation.

In Fig. 10, we illustrate the impact of surface scattering on appearance, particularly in the presence of highlights. Despite an α value that is close to zero, indicating a smooth surface, the subtle perturbations in surface normals significantly contribute to the visual effects around the smoother edges of the highlight and match the photograph well. Here, “Measured” samples directly from the measured normals while TR samples normals from our fit of an analytic normal distribution function using the method by Walter *et al.* [49].

5. DISCUSSION

In this section, we discuss ways to improve the model based on the validation results.

A. Impact of Phase Function

We observed an inability to fully capture the BSSRDF peak (Section 4.A). To explore the influence of the phase function on this peak, we adjusted the mean diameter of the particles from 2.2 μm to 2.23 μm , a seemingly small change that successfully replicated a peak similar to the measurements; see Fig. 11. Despite achieving a matching peak, the overall shape of the BSSRDF simulations still deviates, as in Section 4.A. This experiment underlines the role of the phase function in determining the peak within the irradiated area. It highlights the necessity of an accurate estimate of the particle size distribution to fully predict the characteristics around the peak of the BSSRDFs.

B. Fitting BSSRDF Measurements

In Section 3.D.1, we observed an overestimation of the reflected radiance in both measurements and renderings for

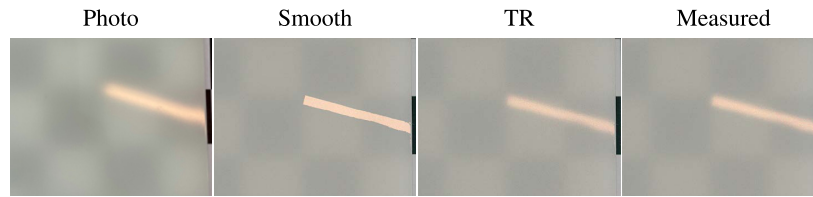


Fig. 10. The visual difference of insurface scattering models for sample IOL1068-08 in the case of reflection highlights. Despite being nearly smooth the small perturbations of surface normals affect the visual appearance around the edges of the highlight. The smooth rendering uses the macroscopic normal, TR samples normals from a fit of the Trowbridge–Reitz distribution, and “Measured” samples directly from the measured normal distribution. The parameters used are from Table 4.

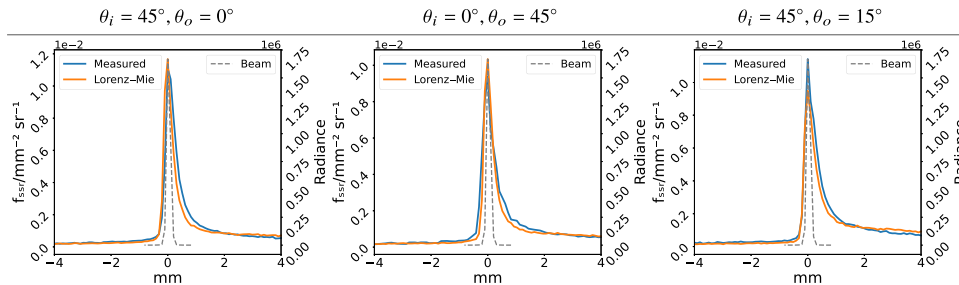


Fig. 11. Cross section along the plane of incidence for simulation and measured for sample IOL1068-08 when the mean-diameter of scattering particles is assumed to be $2.23 \mu\text{m}$.

IOL1068-09. Given the evident overestimation in scattering, our objective is to mitigate this and compute the effective optical properties. The determination of the scattering coefficient is contingent on various factors, including density, particle size, and weight percentage. Without complete information about the scattering particles, this is a high-dimension exploratory task. To simplify this task, we specifically target the weight percentage in this study, acknowledging the potential for adjustments in other parameters to counterbalance each other.

We reduce the weight percentage from its original value of 0.65% to 0.425%. This reduction was chosen to fit with the measured BSSRDF measurement. The simulated BSSRDF slices with this adjusted weight percentage are shown in Fig. 12. The new simulations exhibit a significant decrease in scattering, bringing us much closer to the measurements in terms of both the shape of the BSSRDF isocontours as well as the total energy that is being reflected, see Table 6. However, we also observe that the peak of the simulation is much higher for all three simulations. The exact reason for this is unknown.

It is worth highlighting that we only used the BSSRDF simulation to determine this particle inclusion weight percentage reduction. The advantage of the BSSRDF simulation is that it is orders of magnitude faster than rendering a full image of a 3D

scene. This efficiency enables us to more quickly explore different optical properties. Our manual adjustment is a significant 34.6% decrease, resulting in a correspondingly reduced scattering coefficient of 9606.5 m^{-1} . This reduction also impacts the bulk absorption, which decreases to 9.5117 m^{-1} . The phase function is not affected by this change. Our adjustment of the weight percentage provides valuable insights into the influence of this specific parameter on the overall optical properties.

Figure 13 shows the corresponding renderings with the reduced weight percentage. The error of the rendered images is significantly smaller too, which supports the correspondence between the BSSRDF measurement and the rendered images. Thus, BSSRDF measurement provides an efficient tool for validating optical properties.

C. Limitations

A denser set of BSSRDF measurements would be interesting to further validate our model for several wavelengths and light-view configurations. The images in Fig. 13 still contain some error in the form of a slight color shift. We have not been able to identify the source of this error, but we suspect this difference might be due to the use of refractive indices (including

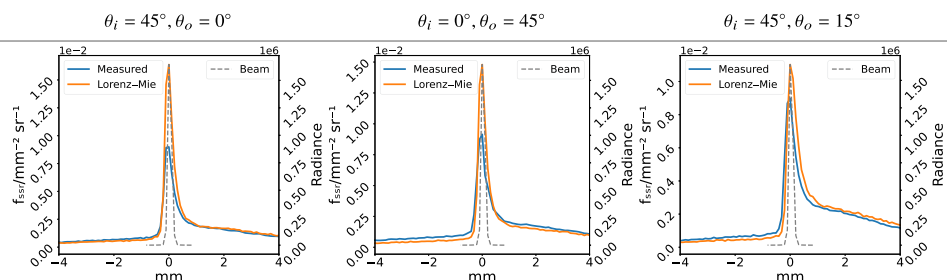
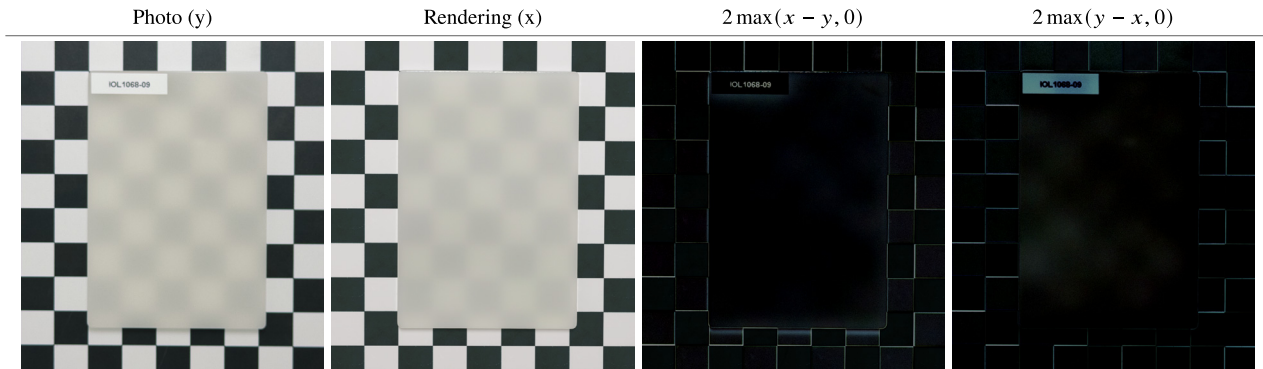


Fig. 12. Cross section along the plane of incidence for simulation and measured for sample IOL1068-09 when the wt-% is decreased to 0.425%.

Table 6. Sum of Radiance from Simulations and Measurements for Sample IOL1068-09 When the wt-% Is Decreased to 0.425%^a

Sample		Angular Configuration		
		$\theta_i = 45^\circ, \theta_o = 0^\circ$	$\theta_i = 0^\circ, \theta_o = 45^\circ$	$\theta_i = 45^\circ, \theta_o = 15^\circ$
IOL1068-09	Measured	8.295	9.982	8.578
	Simulated	7.903 (0.1574)	7.124 (0.3615)	8.106 (0.2399)

^aThe mean squared relative error (MSRE) for simulation against measured BSSRDF in Fig. 5 is denoted in parenthesis.

**Fig. 13.** Comparison of rendered sample IOL1068-09 with photograph when the wt-% is decreased to 0.425%. The RMSE decreased to 0.0537 while SSIM improved to 0.862.

the imaginary part) based on measurements available in the literature.

This leads to another limitation, which is the lack of quantification of errors in the pipeline. Recreating a digital twin requires many separate components and the characterization of each inherits some error. This error feeds into the pipeline, which can enhance error. While we have shown how to validate the components, a challenge in predicting the impact of the error remains. Focus on quantifying this error is an important future endeavor.

In Section 5.B, the weight percentage reduction was carried out manually which requires an iterative labor-intensive process. In the future, an optimization-based inverse rendering technique [22] could be employed instead. We could in this way find changes in model input parameters that would lead to more accurate representation of the BSSRDF and appearance observations. This enables us to estimate a plausible difference between assumed and actual sample properties.

Due to the nature of our samples, we sometimes chose simple models that impose some limits on the samples that our current pipeline can deal with. Fortunately, as mentioned previously, methods exist to extend the applicability of our digitization pipeline as needed. If a sample exhibits a normal distribution with roughness $\alpha > 0.1$, a BSDF model should be used that includes multiple insurface scattering [50]. If the sample to be digitized is very translucent, a correction technique should be used for the 3D scanning of the surface [37]. We consider these options interesting potential extensions of our pipeline that can broaden the range of objects that it can be used to digitize.

6. CONCLUSION

We have proposed digitization and validation pipelines for the appearance of translucent objects. This included an efficient

tool for computing BSSRDF slices for a plane-parallel turbid medium. For insurface scattering, we proposed a modified microfacet distribution function with an ability to account for offsets in the mean microfacet normal angle. For subsurface scattering, we demonstrated the importance of using a more physically based phase function. In general, we have demonstrated how traceable BSSRDF measurements can provide an important tool for validating computed optical properties. The ability to quantitatively assess the accuracy of an object appearance model is the first step toward finding a better model.

Funding. European Metrology Programme for Innovation and Research (18SIB03); Agencia Estatal de Investigación (TED2021-129661B-C21); Innovationsfonden (0223-00041B).

Acknowledgment. The authors would like to thank Covestro AG Deutschland and Rafael Oser for kindly providing us with samples and Klaus Liltorp for 3D scanning our samples. This work has been done in the frame of the EMPIR project 18SIB03 (BxDiff), which has received funding from the EMPIR program co-financed by the participating states and from the European Union's Horizon 2020 Research and Innovation Programme. This publication is part of the project TED2021-129661B-C21, funded by MCIN/AEI/10.13039/501100011033 and by the European Union "NextGenerationEU/PRTR," in which Pablo Santafé-Gabarda and Alejandro Ferrero are involved. Mark Bo Jensen and Jeppe Revall Frisvad would like to acknowledge funding received from Innovation Fund Denmark, project 0223-00041B (ExCheQuER).

Disclosures. The authors declare no conflicts of interest.

Data availability. Data underlying the results and additional results are available at [46].

REFERENCES

- O. S. Alabi, X. Wu, J. M. Harter, *et al.*, "Comparative visualization of ensembles using ensemble surface slicing," *Proc. SPIE* **8294**, 318–329 (2012).
- J. M. Wolfe, N. Klempen, and K. Dahlen, "Postattentive vision," *J. Exp. Psychol. Human Percept. Perform.* **26**, 693–716 (2000).

3. E. K. Vogel, G. F. Woodman, and S. J. Luck, "Storage of features, conjunctions, and objects in visual working memory," *J. Exp. Psychol. Human Percept. Perform.* **27**, 92–114 (2001).
4. P. Santafé-Gabarda, A. Ferrero, N. Tejedor-Sierra, *et al.*, "Primary facility for traceable measurement of the BSSRDF," *Opt. Express* **29**, 34175–34188 (2021).
5. P. Santafé-Gabarda, L. Gevaux, A. Ferrero, *et al.*, "Development and comparison of primary facilities for traceable BSSRDF measurements," *J. Opt.* **26**, 035601 (2024).
6. F. Foschum, F. Bergmann, and A. Kienle, "Precise determination of the optical properties of turbid media using an optimized integrating sphere and advanced Monte Carlo simulations. Part 1: theory," *Appl. Opt.* **59**, 3203–3215 (2020).
7. F. Bergmann, F. Foschum, R. Zuber, *et al.*, "Precise determination of the optical properties of turbid media using an optimized integrating sphere and advanced Monte Carlo simulations. Part 2: experiments," *Appl. Opt.* **59**, 3216–3226 (2020).
8. C. Sun, B. Aernouts, and W. Saeys, "Bridging the gap between measurement-based and simulation-based metamodels for deriving bulk optical properties from spatially-resolved reflectance profiles: effect of illumination and detection geometry," *Opt. Express* **29**, 15882–15905 (2021).
9. D. Sun, X. Wang, M. Huang, *et al.*, "Estimation of optical properties of turbid media using spatially resolved diffuse reflectance combined with LSTM-attention network," *Opt. Express* **31**, 10260–10272 (2023).
10. J. D. Stets, A. D. Corso, J. B. Nielsen, *et al.*, "Scene reassembly after multimodal digitization and pipeline evaluation using photorealistic rendering," *Appl. Opt.* **56**, 7679–7690 (2017).
11. M. Hannemose, M. E. B. Doest, A. Luongo, *et al.*, "Alignment of rendered images with photographs for testing appearance models," *Appl. Opt.* **59**, 9786–9798 (2020).
12. A. Ferrero, J. R. Frisvad, L. Simonot, *et al.*, "Fundamental scattering quantities for the determination of reflectance and transmittance," *Opt. Express* **29**, 219–231 (2021).
13. T. J. Farrell, M. S. Patterson, and B. Wilson, "A diffusion theory model of spatially resolved, steady-state diffuse reflectance for the noninvasive determination of tissue optical properties in vivo," *Med. Phys.* **19**, 879–888 (1992).
14. L. Wang and S. L. Jacques, "Use of a laser beam with an oblique angle of incidence to measure the reduced scattering coefficient of a turbid medium," *Appl. Opt.* **34**, 2362–2366 (1995).
15. A. Kienle, L. Lilge, M. S. Patterson, *et al.*, "Spatially resolved absolute diffuse reflectance measurements for noninvasive determination of the optical scattering and absorption coefficients of biological tissue," *Appl. Opt.* **35**, 2304–2314 (1996).
16. S. A. Prahl, M. J. van Gemert, and A. J. Welch, "Determining the optical properties of turbid media by using the adding-doubling method," *Appl. Opt.* **32**, 559–568 (1993).
17. H. C. van de Hulst, *Light Scattering by Small Particles* (Wiley, 1957).
18. C. F. Bohren and D. R. Huffman, *Absorption and Scattering of Light by Small Particles* (Wiley, 1983).
19. R. W. Preisendorfer, *Radiative Transfer on Discrete Spaces* (Pergamon, 1965).
20. W. H. Venable, Jr. and J. J. Hsia, "Optical radiation measurements: describing spectrophotometric measurements," Technical Report NBS TN 594-9 (National Bureau of Standards, 1974).
21. J. R. Frisvad, S. A. Jensen, J. S. Madsen, *et al.*, "Survey of models for acquiring the optical properties of translucent materials," *Comput. Graph. Forum* **39**, 729–755 (2020).
22. I. Gkioulekas, S. Zhao, K. Bala, *et al.*, "Inverse volume rendering with material dictionaries," *ACM Trans. Graph.* **32**, 162:1–13 (2013).
23. T. Iser, T. Rittig, E. Nogué, *et al.*, "Affordable spectral measurements of translucent materials," *ACM Trans. Graph.* **41**, 199:1–13 (2022).
24. H. W. Jensen, S. R. Marschner, M. Levoy, *et al.*, "A practical model for subsurface light transport," in *Proceedings of SIGGRAPH* (ACM, 2001), pp. 511–518.
25. T. G. Andersen, V. Falster, J. R. Frisvad, *et al.*, "Hybrid fur rendering: combining volumetric fur with explicit hair strands," *Vis. Comput.* **32**, 739–749 (2016).
26. Z. Velinov, M. Papas, D. Bradley, *et al.*, "Appearance capture and modeling of human teeth," *ACM Trans. Graph.* **37**, 207:1–13 (2018).
27. B. Nicolet, F. Rousselle, J. Novak, *et al.*, "Recursive control variates for inverse rendering," *ACM Trans. Graph.* **42**, 62:1–13 (2023).
28. Z. Zhang, N. Roussel, and W. Jakob, "Projective sampling for differentiable rendering of geometry," *ACM Trans. Graph.* **42**, 212:1–212:14 (2023).
29. X. Deng, F. Luan, B. Walter, *et al.*, "Reconstructing translucent objects using differentiable rendering," in *SIGGRAPH 2022 Conference Proceedings* (ACM, 2022), pp. 38:1–38:10.
30. D. Gao, G. Chen, Y. Dong, *et al.*, "Deferred neural lighting: free-viewpoint relighting from unstructured photographs," *ACM Trans. Graph.* **39**, 258:1–15 (2020).
31. C. Zeng, G. Chen, Y. Dong, *et al.*, "Relighting neural radiance fields with shadow and highlight hints," in *SIGGRAPH 2023 Conference Proceedings* (ACM, 2023), pp. 73:1–73:11.
32. H.-X. Yu, M. Guo, A. Fathi, *et al.*, "Learning object-centric neural scattering functions for free-viewpoint relighting and scene composition," *Trans. Mach. Learn. Res.* (2023).
33. S. Zhu, S. Saito, A. Bozic, *et al.*, "Neural relighting with subsurface scattering by learning the radiance transfer gradient," *arXiv*, arXiv:2306.09322 [cs.CV] (2023).
34. J. Geng, "Structured-light 3D surface imaging: a tutorial," *Adv. Opt. Photon.* **3**, 128–160 (2011).
35. M. Kazhdan and H. Hoppe, "Screened Poisson surface reconstruction," *ACM Trans. Graph.* **32**, 29:1–13 (2013).
36. M. G. Guerra, S. S. Gregersen, J. R. Frisvad, *et al.*, "Measurement of polymers with 3D optical scanners: evaluation of the subsurface scattering effect through five miniature step gauges," *Meas. Sci. Technol.* **31**, 015010 (2019).
37. Q. Zhang, F. Liu, L. Lu, *et al.*, "Reconstruction of transparent objects using phase shifting profilometry based on diffusion models," *Opt. Express* **32**, 13342–13356 (2024).
38. X. Zhang, J. Qiu, X. Li, *et al.*, "Complex refractive indices measurements of polymers in visible and near-infrared bands," *Appl. Opt.* **59**, 2337–2344 (2020).
39. T. Siefke, S. Kroker, K. Pfeiffer, *et al.*, "Materials pushing the application limits of wire grid polarizers further into the deep ultraviolet spectral range," *Adv. Opt. Mater.* **4**, 1780–1786 (2016).
40. T. König, P. Ledin, J. Kerszulis, *et al.*, "Electrically tunable plasmonic behavior of nanocube-polymer nanomaterials induced by a redox-active electrochromic polymer," *ACS Nano* **8**, 6182–6192 (2014).
41. S. Chandrasekhar, *Radiative Transfer* (Clarendon, 1950). Unabridged and slightly revised version published by Dover in 1960.
42. L. C. Henyey and J. L. Greenstein, "Diffuse radiation in the galaxy," *Astrophys. J.* **93**, 70–83 (1940).
43. L. Lorenz, "Lysbevægelsen i og uden for en af plane lysbølger belyst kugle," *K. Dan. Vidensk. Selsk. Skr.* **6**, 1–62 (1890).
44. G. Mie, "Beiträge zur optik trüber medien, speziell kolloidaler metallösungen," *Ann. Phys.* **330**, 377–445 (1908).
45. J. R. Frisvad, N. J. Christensen, and H. W. Jensen, "Computing the scattering properties of participating media using Lorenz-Mie theory," *ACM Trans. Graph.* **26**, 60:1–10 (2007).
46. <https://eco3d.compute.dtu.dk/pages/bxdiff>.
47. K. E. Torrance and E. M. Sparrow, "Theory for off-specular reflection from roughened surfaces," *J. Opt. Soc. Am.* **57**, 1105–1114 (1967).
48. J. Stam, "An illumination model for a skin layer bounded by rough surfaces," in *Rendering Techniques 2001 (EGWR)* (Springer, 2001), pp. 39–52.
49. B. Walter, S. R. Marschner, H. Li, *et al.*, "Microfacet models for refraction through rough surfaces," in *Proceedings of EGSR'07* (Eurographics Association, 2007), pp. 195–206.
50. E. Heitz, J. Hanika, E. d'Eon, *et al.*, "Multiple-scattering microfacet BSDFs with the Smith model," *ACM Trans. Graph.* **35**, 58:1–14 (2016).
51. D. Sforza and F. Pellacini, "Numerical approximations for energy preserving microfacet models," *Comput. Graph.* **114**, 36–44 (2023).
52. B. Wittmann, P. Montmitonnet, A. Burr, *et al.*, "BRDF and gloss computation of polyurethane coatings from roughness measurements: modelling and experimental validation," *Prog. Org. Coat.* **156**, 106247 (2021).
53. B. Smith, "Geometrical shadowing of a random rough surface," *IEEE Trans. Antennas Propag.* **15**, 668–671 (1967).

54. P. Beckmann and A. Spizzichino, *The Scattering of Electromagnetic Waves from Rough Surfaces* (Pergamon, 1963).
55. T. S. Trowbridge and K. P. Reitz, "Average irregularity representation of a rough surface for ray reflection," *J. Opt. Soc. Am.* **65**, 531–536 (1975).
56. F. Xie, J. Bieron, P. Peers, *et al.*, "Experimental analysis of multiple scattering BRDF models," in *SIGGRAPH Asia 2021 Technical Communications (ACM)* (2021), pp. 13:1–13:4.
57. Z. Dong, B. Walter, S. Marschner, *et al.*, "Predicting appearance from measured microgeometry of metal surfaces," *ACM Trans. Graph.* **35**, 9:1–13 (2016).
58. M. Pharr, W. Jakob, and G. Humphreys, *Physically Based Rendering: From Theory to Implementation*, 4th ed. (MIT, 2023).
59. J. R. Frisvad, "Importance sampling the Rayleigh phase function," *J. Opt. Soc. Am. A* **28**, 2436–2441 (2011).
60. <https://hnmnart.github.io/#/Simulator>.
61. J. R. Frisvad, N. J. Christensen, and H. W. Jensen, "Predicting the appearance of materials using Lorenz-Mie theory," in *The Mie Theory: Basics and Applications* (Springer, 2012), chap. 4, pp. 101–133.
62. S. G. Parker, J. Bigler, A. Dietrich, *et al.*, "OptiX: a general purpose ray tracing engine," *ACM Trans. Graph.* **29**, 66:1–13 (2010).
63. A. Stockman and L. T. Sharpe, "The spectral sensitivities of the middle- and long-wavelength-sensitive cones derived from measurements in observers of known genotype," *Vis. Res.* **40**, 1711–1737 (2000).
64. Z. Zhang, "A flexible new technique for camera calibration," *IEEE Trans. Pattern Anal. Mach. Intell.* **22**, 1330–1334 (2000).